Chapter xxx

Coupled viscoplastic damage model for hypervelocity impact induced damage in metals and composites

George Z. Voyiadjis
Department of Civil and Environmental Engineering,
Louisiana State University, Baton Rouge, Louisiana, USA
voyiadjis@eng.lsu.edu

Babur Deliktas
Department of Civil Engineering
Mustafa Kemal University, Hatay, Turkey
bdeliktas@mku.edu.tr

Farid H. Abed
Department of Civil Engineering
College of Engineering, American University of Sharjah, Sharjah,
United Arab Emirates
E-mail:fabed@aus.edu

Rashid K. Abu Al-Rub
Zachary Department of Civil Engineering, Texas A&M University
College Station, TX 77843-3136
E-mail: rabualrub@civil.tamu.edu

1. Introduction

The recent advances in aerospace and war capabilities have made necessary the modification of the design of structures that are prone to hypervelocity impact in order to increase their resistancy against the penetration and perforation by projectiles with much higher impact energies. In this respect, high performance materials need to be developed so that they can offer significant advantages over the currently used materials. Metals and Composites are among those materials that are often used in various parts of the structural components of the engineering structure in aerospace, automobile and defense industries. In general, these materials are subjected to tremendous microstructural changes due to perforation and penetration phenomena and have complex material response due to a strong rate and temperature dependence when deformed non-uniformly into the inelastic range. Therefore, the high velocity impacting mechanism needs to be understood properly in order to be able to design materials of high ballistic resistant response. However, the exact mechanism by which the impacting target materials undergo fracture and ablation is a relatively complex process [1]. Generally, strong shock wave-material interactions are generated and propagated along both the projectile and the target, which can lead to fracture at low global inelastic strains.

Many researchers, therefore, have investigated the material failure mechanism during high velocity impact conditions with the ultimate goal of developing a micromechanical constitutive model that can effectively simulate the impact damage problem (see e.g. [2–11]).

Finite element computational models emerged as accurate tools to investigate the mechanical behavior of structural materials due to their ability to include complex constitutive equations [12-17]. Currently many non commercial/commercial finite element package programs are available to simulate the challenging engineering problems in conjunction with either built in material models or the user defined material routines. Modeling and simulation of the perforation and penetration problem due to impacting a plate with a projectile has been one of those complex challenging engineering problems of the field of computational solid mechanics [18-21]. This is due to the fact that such problems involve multiple structural and material responses such as dynamic behavior, damage, fracture, rate and temperature dependent behavior, contact and friction [22, 23]. In terms of the phenomenological models several constitutive models exist [2, 24-27]. Arias et. al [22] used the Johnson-Cook model (JC) [2] to simulate the behavior of the thermoviscoplastic behavior of the material constituting the plate subjected to impact by various projectiles having different shapes for the range of impact velocities from 190 to 600m/s. Manzenmiller-Lubliner-Taylor [28] continuum damage theory along with cohesive crack model is used by Arevola et. al

[29] to predict the energy absorption capacity of the C/epoxy laminated composite plate subjected to the low velocity impact. Ji et. al [30] used the unit cell model of 3D woven composites by incorporating the damage model via user material subroutine VUMAT into ABAQUS/explicit to predict the impact damage response of the composite plate. Lee et al. [31] investigated the penetration and perforation behavior of the metal matrix composite by using the simulation of LS-DYNA3D where they assumed that the matrix of the composite is elastic-plastic whereas the reinforcing fiber is the Chang-Chang [32] composite failure model. Some experimental and theoretical issues of the perforation and penetration problems of the laminated metal matrix composite materials have been discussed extensively in the literature. For example, the experimental study conducted on the perforation of GRP (E-glass/phenonic) laminates struck by an ogival-nosed AP projectile with high velocity impact was performed by Kumar and Bhat [33] and Kumar et al. [34]. However, most of the phenomenological models similar to those used in the previous studies listed here are quite accurate at low temperatures on the other hand at high temperatures and under high strain rate conditions the accuracy in their predictions of these models show quite large variations [35].

The key role in the numerical simulation of the impact damage related problems is the accurate modeling of the material behavior at high strain rates and temperatures. It is noted that none of these constitutive models address the problem of describing high shock compression and subsequent material degradation and failure in which the latter is expressed as an evolving micro-flaw having a damage rate determined from micro-mechanical analysis. Moreover, these models cannot consider the actual sizes, shapes, and orientations of the individual micro-voids and micro-cracks, which may have a predominant influence on the mechanical response of the material. The mechanical behavior of these applications cannot be characterized by classical (rate-independent) continuum theories because they incorporate no ‘material length scales’. It is therefore necessary to develop a coupled rate-dependent (viscoplasticity) continuum damage theory bridging the gap between the classical continuum theories and the microstructure simulations.

The authors of this work have recently recognized the need for a micro-mechanical damage model that accounts for the nonlocal microscopic interactions between material points (i.e. to take into account the influence of an internal state variable at a point on its neighborhood) in the simulation of metals and metal matrix composites impact problems [36–40]. This nonlocal microdamage model is formulated based on the enhanced gradient-dependent theory which is successful in explaining the size effects encountered at the micron scale and in preserving the well-posed nature of the initial boundary value problem that governs the solution of material instability triggering strain localization (see Voyiadjis et al. [36, 37] and Abu Al-Rub and Voyiadjis [37]). Moreover, the viscoplasticity theory (rate-dependency) allows the spatial difference operator in the governing equations to retain its ellipticity and consequently the initial boundary value problem is hence well-posed (see e.g. [41–48]). However, the gradient dependent theories enhance a stronger regularization of the localization problem than the rate-dependent theory. Moreover, the rate-dependent theory cannot explain the size effect of the

microdamage zone (i.e. the void/crack size and spacing) on the material failure while the gradient theory can address that. Therefore, the objective of this work is to present for high speed impact damage problems a novel microdamage constitutive model that possesses several material length scales. This model can be used to produce physically meaningful and numerically converging results within strain localization computations by finite element codes. Moreover, the algorithmic aspects and numerical implementation of this model in finite element codes are presented in this chapter.

The outline of this paper is as follows: in section 2, general mechanisms of the perforation and penetration mechanisms are discussed. In section 3 a coupled rate-dependent (viscoplasticity) continuum damage theory is presented. In section 4, the proposed elastic predictor and coupled viscoplastic-viscodamage corrector algorithm that allows for total uncoupling of geometrical and material nonlinearities are presented. The nonlinear algebraic system of equations is solved by consistent linearization and the Newton–Raphson iteration. In section 5, numerical simulations of material instability are introduced in order to validate and test the proposed finite strain approach along with the proposed algorithm and its implementation in the ABAQUS finite element code. Experimental comparisons of the adiabatic shear localizations between the proposed model simulations and other independent results are presented. Effect of initial temperatures and loading rates on the development of shear localizations is also investigated in this section. In this regard shear localizations in cylindrical hat-shaped samples was investigated and comparisons with experimental results were presented [62]. Model capabilities were preliminarily illustrated for the dynamic localization of inelastic flow in adiabatic shear bands and compared with the experimental results of Borvik et al. [9] for the perforation of 12mm thick Weldox 460E steel plates by deformable blunt projectiles at various impact speeds [13]. Numerical simulation was also performed in order to investigate penetration and perforation of a projectile impacting a metal matrix composite plate [39].

2. Theoeritical Prelimniraies for High velocity impact

2.1. Penetration and perforation mechanisms

The penetration and perforation mechanisms are interdisciplinary subjects and are based on the laws of conservation and compatibility. Penetration implies movement of a projectile into a target. Phenomenologically, as illustrated in Fig. 1, the penetration can be viewed as a process to generate a cone shaped macro crack in the material, in which, the kinetic energy of the penetrator is dissipated.

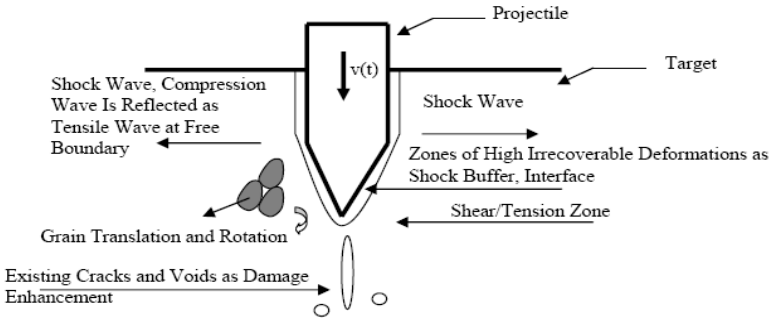

Figure 1: Schematics illustration the penetration process [13].

Perforation implies penetration all the way through a target. Projectile exit through a finite target is often accompanied by delamination and plugging. Delamination refers to a tensile failure parallel to the target rear surface and is often initiated by spall. However, it can also occur in quite thick targets, where it seems to be caused by *shear bands* around the projectile head that can propagate as cracks near the exit surface [49].

In general, a penetration equation is a set of equations that are used to predict the outcome of an important event, such as the residual velocity or mass of the projectile after impact. Empirical penetration equations are essentially curve fits and take the general form $f\left(x_1, x_2, \ldots, x_n\right)$ where $x_1, x_2, \ldots, x_n$ are parameters such as projectile size and target thickness. It is important to note that results of these equations are only accurate if the case for which it is being used is close to that of the experimental data to which the equations are fit [50]. Prediction of the Ballistic limit is a very difficult task for which complete success may not be possible. Therefore, extensive experimental work is being done to date to understand which parameters affect the impact in composite structures. The analysis is still complex because the events that occur at the projectile/target interface are somewhat unknown. Although many studies have been performed, only highly controlled velocities, shape, sizes and trajectories have been examined. As a result, numerous approximations and assumptions must be made in order to apply to these analyses. Impact is a much localized phenomenon. Stress and strain effects are usually limited to within 3-6 projectile diameters of the impacted zone [49]. Impacted target materials may fail by a combination of several modes including spalling, plugging, petaling, ductile or brittle fracture, and adiabatic shearing.

Spalling is the tensile failure of the target material due to reflection of the initial compressive waves from the far side of the target. Failure by spalling can occur on either the front or back of a target and is characterized by the formation of

petals or ejects. In the event of impact there is an exchange of energy that takes place:

$$E_{\text{tans}} = E_{\text{plate}}^{\text{internal}} + E_{\text{plate}}^{\text{kinetic}} + E_{\text{eroded}}^{\text{internal}} + E_{\text{eroded}}^{\text{kinetic}} \quad (1)$$

Law of conservation is observed in any physical phenomena. Kinetic energy of the projectile is spent in raising the internal energy and kinetic energy of the plate and some part of the energy is lost in the form of eroded material. The amount of energy dissipated also differs with geometry. Blunt projectiles like cylinders are found to cause plugging because of pure shear failure, while the conical projectiles are found to cause petaling effects.

High velocity impact will localize compression of the composite and subsequently shearing the fiber and spalling of the resin during impact. Once the projectile has slowed, the composite deforms causing fiber stretching, pullout and delamination of the composite layers and thus lower the load carrying capacity.

3.A coupled rate-dependent (viscoplasticity) continuum damage theory

In this section a general theoretical framework for the analysis of heterogeneous media that assesses a strong coupling between rate-dependent plasticity and anisotropic rate-dependent damage is presented for high velocity impact related problems. The developed framework is based on thermodynamic laws, nonlinear continuum mechanics, and nonlocal gradient-dependent theory [36– 39]. This model uses a combined viscosity and nonlocal gradient localization limiters in order to regularize the dynamic strain localization problems. Material length scales are incorporated explicitly through the nonlocal gradient theory and implicitly through the rate-dependency (viscoplasticity). The proposed formulation includes hypoelasto-thermo-viscoplasticity with anisotropic thermoviscodamage; a dynamic yield criterion; a dynamic damage growth criterion; non-associated flow rules; thermal softening; nonlinear strain hardening; strain-rate hardening; strain hardening gradients; strain-rate hardening gradients; and an equation of state. The idea of bridging length scales is made more general and complete by introducing spatial higher-order gradients in the temporal evolution equations of the internal state variables that describe hardening in coupled viscoplasticity and viscodamage models. The model is mainly developed to regularize the ill-posed problem caused by strain-softening material behavior and to incorporate the size effect (size and spacing of micro-defects) in material behavior for high velocity impact damage related problems.

Generally, three sets of equations are needed to simulate the impact damage problems: a yield criterion that incorporates the strain rate and temperature effects on the material's strength, an equation of state which accounts for material pressure sensitivity, and a damage model which is needed to simulate progressive failure and fracture. The coupled constitutive model of viscoplasticity and ductile viscodamage

(rate-dependent damage) is used to predict the material behavior under dynamic loading conditions. It was earlier derived based on the laws of thermodynamics [36–39] and combines all these requirements. Only the main governing constitutive equations will be given in the following. The model is based on the nonlocal gradient plasticity and gradient damage theories. It includes the nonlocal von Mises yield criterion, the non-associated flow rules, isotropic and anisotropic strain hardening, strain rate hardening, softening due to adiabatic heating and anisotropic damage evolution, and finally a path dependent equation of state. The stress-strain rate relationship in the spatial and damaged configuration is given by

$$\overset{\nabla}{\boldsymbol{\tau}} = \mathbb{C} : \left(\boldsymbol{d} - \boldsymbol{d}^{vp} - \boldsymbol{d}^{vd} \right) - \boldsymbol{A} : \overset{\nabla}{\hat{\boldsymbol{\phi}}} - \mathbb{C} : \alpha_t \dot{T} \mathbf{1} \tag{2}$$

where

$$\mathbb{C} = \hat{\boldsymbol{M}}^{-1} : \bar{\mathbb{C}} : \hat{\boldsymbol{M}}^{-1} \text{ and } \hat{\boldsymbol{M}} = 2\left[\left(\mathbf{1} - \hat{\boldsymbol{\phi}} \right) \otimes \mathbf{1} + \mathbf{1} \otimes \left(\mathbf{1} - \hat{\boldsymbol{\phi}} \right) \right]^{-1} \tag{3}$$

The notation, $\overset{\nabla}{}$ indicates co-rotational objective derivative, $\boldsymbol{\tau}$ is the Kirchhoff stress tensor, $\boldsymbol{d}$ is the total rate of deformation, $\boldsymbol{d}^{vp}$ is the viscoplastic rate of deformation, $\boldsymbol{d}^{vd}$ is the viscodamage rate of deformation, $\bar{\mathbb{C}}$ and $\mathbb{C}$ are the fourth-order undamaged and damaged elasticity tensors respectively, α_t is the thermal expansion coefficient, $\dot{T}$ is the rate of absolute temperature, and $\mathbf{1}$ is the second-order identity tensor. The fourth-order tensors $\bar{\mathbb{C}}$ and $\boldsymbol{A}$ are given by the following relations:

$$\begin{gathered} \bar{\mathbb{C}} = K^e \mathbf{1} \otimes \mathbf{1} + 2G^e \mathbf{I}^{dev}, \\ \boldsymbol{A} = \frac{\partial \hat{\boldsymbol{M}}^{-1}}{\partial \hat{\boldsymbol{\phi}}} : \hat{\boldsymbol{M}} : \boldsymbol{\tau} + \mathbb{C} : \hat{\boldsymbol{M}} : \frac{\partial \hat{\boldsymbol{M}}^{-1}}{\partial \hat{\boldsymbol{\phi}}} : \mathbb{C}^{-1} : \left[\boldsymbol{\tau} + \alpha_t \left(T - T_r \right) \mathbf{1} \right] \end{gathered} \tag{4}$$

where K^e is the bulk modulus, G^e is the shear modulus, T_r is the reference temperature, and $\mathbf{I}^{dev}$ is the deviatoric part of the fourth-order identity tensor $\mathbf{I}$. In the undamaged configuration, Eq. (2) can be written as follows:

$$\overset{\nabla}{\bar{\boldsymbol{\tau}}} = \bar{\mathbb{C}} : \left(\bar{\boldsymbol{d}} - \bar{\boldsymbol{d}}^{vp} \right) - \alpha_t \dot{T} \mathbf{1} \tag{5}$$

Note that hereafter $(:)$ stands for tensor contraction, the superimposed dot $(\cdot)$ indicates the differentiation with respect to time, t, the superimposed hat indicates a nonlocal quantity, the superimposed dash indicates a quantity in the undamaged (effective) configuration, and $\otimes$ denotes the dyadic product.

Materials with microstructure are nonlocal in behavior due to the interplay of characteristic lengths including sizes or spacing of defect clusters (e.g. micro-cracks, micro-voids, dislocations). As traditional continuum mechanics does not contain characteristic lengths, the use of the nonlocal concept is required in order to incorporate a microstructural length scale that introduces long-range microstructural interactions where the stress response at a material point is assumed to depend on the state of its neighborhood in addition to the state of the material point itself. Moreover, this length scale preserves the well-posed nature of the initial boundary

value problem governing the solution of material instability triggering strain localization. In the following, the nonlocality is incorporated through the use of the gradient-dependent theory such that if $\boldsymbol{\phi}$ is some 'local' field in a domain *V*, the corresponding nonlocal field, $\hat{\phi}$, is defined as follows:

$$\hat{\boldsymbol{\phi}} = \boldsymbol{\phi} + \tfrac{1}{2}\ell^2\nabla^2\boldsymbol{\phi} \tag{6}$$

where ℓ is the *internal material length scale*, which weights each component of the gradient term identically, and ∇^2 is the Laplacian operator. The length scale ℓ should be obtained from gradient-dominant experiments such as indentation tests, bending tests, or torsion tests [51–53]. The role of the material length scale in solving the impact damage problem and in preserving the objectivity of the continuum modeling and numerical simulation of the localization problem is the main concern of this paper. The first-order gradients are disregarded since the isotropic nonlocal influence is assumed. The viscoplastic rate of deformation, $\boldsymbol{d}^{vp}$, the viscodamage rate of deformation, $\boldsymbol{d}^{vd}$, the rate of the second-order damage tensor $\boldsymbol{\phi}$, and viscoplastic rate of deformation in the undamaged configuration, $\bar{\boldsymbol{d}}^{vp}$, are given as follows:

$$\boldsymbol{d}^{vp} = \dot{\lambda}^{vp}\frac{\partial f}{\partial \boldsymbol{\tau}},\ \boldsymbol{d}^{vd} = \dot{\lambda}^{vd}\frac{\partial g}{\partial \boldsymbol{\tau}},\ \overset{\nabla}{\boldsymbol{\phi}} = \dot{\lambda}^{vp}\frac{\partial f}{\partial \boldsymbol{Y}} + \dot{\lambda}^{vd}\frac{\partial g}{\partial \boldsymbol{Y}},\ \bar{\boldsymbol{d}}^{vp} = \dot{\lambda}^{vp}\frac{\partial f}{\partial \bar{\boldsymbol{\tau}}} \tag{7}$$

where the potentials f and g are the nonlocal viscoplastic and viscodamage conditions given in the undamaged (effective) configuration, respectively, by

$$f = \sqrt{\tfrac{3}{2}\left(\bar{\boldsymbol{\tau}}' - \hat{\bar{\boldsymbol{X}}}\right):\left(\bar{\boldsymbol{\tau}}' - \hat{\bar{\boldsymbol{X}}}\right)} - [\bar{Y}_{yp} + \hat{\bar{R}}(\bar{p})][1 + (\eta^v\dot{\bar{p}})^{1/m}][1 - (T/T_m)^n] \le 0 \tag{8}$$

and

$$g = \sqrt{\left(\hat{\boldsymbol{Y}} - \hat{\boldsymbol{H}}\right):\left(\hat{\boldsymbol{Y}} - \hat{\boldsymbol{H}}\right)} - [r_o + \hat{K}(\hat{r})][1 + (\eta^v\dot{\bar{p}})^{1/m}][1 - (T/T_m)^n] \le 0 \tag{9}$$

where $\bar{\boldsymbol{\tau}}'$ is the effective deviatoric stress tensor; $\bar{Y}_{yp}$ is the initial yield strength (at zero absolute temperature, zero plastic strain, and static strain rate); $\hat{\bar{R}}(\bar{p})$ is the nonlocal isotropic hardening function; $\hat{\bar{\boldsymbol{X}}}$ is the nonlocal anisotropic (kinematic) hardening stress; $\bar{p} = \int_0^t \sqrt{\tfrac{2}{3}\bar{d}_{ij}^{vp}\bar{d}_{ij}^{vp}}\,\mathrm{d}t$ is the effective accumulative viscoplastic strain; m and n are material constants; η^v is the relaxation time; the nonlocal damage forces $\hat{\boldsymbol{Y}}$ and $\hat{K}(\hat{r})$ are, respectively, characterizing the energy release rate and the damage isotropic hardening function; r_o is the initial damage threshold; $\hat{r} = \sqrt{\hat{\boldsymbol{\phi}}:\hat{\boldsymbol{\phi}}}$ is the nonlocal damage accumulation; and T_m is the melting temperature.

The viscoplastic and viscodamage multipliers, $\dot{\lambda}^{vp}$ and $\dot{\lambda}^{vd}$, can be obtained in a nonlocal sense using the following generalized Kuhn-Tucker conditions for rate-dependent problems such that

$$\dot{\lambda}^{vp} \geq 0, \quad f \leq 0 \;\Leftrightarrow \dot{\lambda}^{vp} f = 0 \quad \text{and} \quad \dot{\lambda}^{vd} \geq 0, \quad g \leq 0 \;\Leftrightarrow \dot{\lambda}^{vd} g = 0 \tag{10}$$

The nonlocal evolution equation for the isotropic and kinematic hardening in the undamaged configuration, are given respectively by:

$$\dot{\bar{R}} = \dot{\bar{R}} + \tfrac{1}{2}\ell^2\nabla^2\dot{\bar{R}} \quad \text{with} \quad \dot{\bar{R}} = \frac{a_1\dot{\lambda}^{vp}}{\left(1-\bar{r}\right)^2}\left(1-k_1\bar{\bar{R}}\right) \tag{11}$$

and

$$\overset{\nabla}{\bar{\boldsymbol{X}}} = \overset{\nabla}{\bar{\boldsymbol{X}}} + \tfrac{1}{2}\ell^2\nabla^2\overset{\nabla}{\bar{\boldsymbol{X}}} \quad \text{with} \quad \overset{\nabla}{\bar{X}}_{ij} = a_2\dot{\lambda}^{vp}\hat{\boldsymbol{M}} : \hat{\boldsymbol{M}} : \left(\frac{\partial f}{\partial \bar{\boldsymbol{\tau}}} - k_2\bar{\bar{\boldsymbol{X}}}\right) \tag{12}$$

The evolution equations for the nonlocal viscodamage isotropic and kinematic hardening functions respectively are given by

$$\dot{\bar{K}} = \dot{K} + \tfrac{1}{2}\ell^2\nabla^2\dot{K} \quad \text{with} \quad \dot{K} = a_3\dot{\lambda}^{vd}\left(1-h_1\bar{K}\right) \tag{13}$$

and

$$\overset{\nabla}{\hat{\boldsymbol{H}}} = \overset{\nabla}{\boldsymbol{H}} + \tfrac{1}{2}\ell^2\nabla^2\overset{\nabla}{\boldsymbol{H}} \quad \text{with} \quad \overset{\nabla}{\boldsymbol{H}} = a_4\dot{\lambda}^{vd}\left(\frac{\partial g}{\partial \boldsymbol{Y}} - h_2\hat{\boldsymbol{H}}\right) \tag{14}$$

The nonlocal strain energy release rate is given by

$$\hat{\boldsymbol{Y}} = \frac{1}{2}\left[\boldsymbol{\tau} - \alpha_t\left(T-T_r\right)\mathbf{1}\right] : \hat{\boldsymbol{M}} : \frac{\partial \hat{\boldsymbol{M}}^{-1}}{\partial \hat{\boldsymbol{\phi}}} : \mathbb{C}^{-1} : \left[\boldsymbol{\tau} + \alpha_t\left(T-T_r\right)\mathbf{1}\right] \tag{15}$$

where k_i, h_i, and a_i (i=1-4) are material constants that can be identified from conventional tests (e.g. uniaxial tension test).

Equation of state is a thermodynamic equation describing the state of matter under a given set of physical conditions. In this sense the thermodynamic pressure stress P for a shock compressed solid is given as follows:

$$P = \left(1-\gamma\right)c_v T^{ig}\varepsilon^e \tag{16}$$

where

$$T^{ig} = T_r \exp\left[\left(\eta-\eta_r\right)/c_v\right]\left[1+\varepsilon^e\right]^{(\gamma-1)} \exp\left[\left(\gamma-1\right)\left(1/\left(1+\varepsilon^e\right)-1\right)\right] \tag{17}$$

which gives the equation of state necessary for high-impact loading. The equation of state accounts for compressibility effects (changes in density) and irreversible thermodynamic processes. The parameter $\gamma = c_p/c_v$ is the ratio of the specific heats, where c_p and c_v are the specific heats at constant pressure and constant volume, respectively, $\varepsilon^e = 1/J^e - 1$ is the nominal elastic volumetric strain where $J^e = \det(\boldsymbol{F}^e)$ is the determinant of the elastic deformation gradient $\boldsymbol{F}^e$, T^{ig} is chosen to have the form of ideal gas temperature, and η is the entropy, which is expressed by

$$\eta = \eta_r + \frac{3}{\rho_o} K^e \alpha_t \boldsymbol{e}^e : \mathbf{1} + c_p \left(T - T_r \right) \tag{18}$$

In the above relation, η_r is the reference entropy, ρ_o is the reference density, and $\boldsymbol{e}^e$ is the Eulerian elastic strain tensor.

To establish the actual heat generation that occurs during the highly transient impact events of the thermo-mechanically coupled finite element, the development of a heat equation is imperative. However, because the whole impact process lasts a few hundred of a μs, the effect of heat conduction is negligible over the domain of the specimen and therefore, an adiabatic condition is assumed such that the increase in temperature is calculated by the following heat equation:

$$\rho_o c_p \dot{T} = \Upsilon \boldsymbol{\tau}' : \left(\boldsymbol{d}^{vp} + \boldsymbol{d}^{vd} \right) + J^e P(\boldsymbol{d}^e : \mathbf{1}) \tag{19}$$

In this development one bases the failure criterion on the nonlocal evolution of the accumulated microdamage internal state variable, $\widehat{\boldsymbol{\phi}}$, and the equation of state for the thermodynamic pressure. It implies that for

$$\left\| \widehat{\phi} \right\| = \sqrt{\widehat{\phi}_{ij} \widehat{\phi}_{ij}} \geq \left\| \phi \right\|_c \quad \text{and/or} \quad P \geq P_{cutoff} \tag{20}$$

the material loses its carrying capacity, where $\| \phi \|_c$ is the critical damage when catastrophic failure in the material takes place and P_{cutoff} is the pressure cutoff value when tensile failure or compressive failure occurs.

Many authors tend to use a constant value for the length scale parameter and neglect its variation with the state of loading. For example, the damage zone ahead of the crack tip or the mean dislocation spacing will decrease with increasing strain rate and increase with decreasing temperature, which for small scale yielding is of the order of microns. This causes the intrinsic material length scale to decrease with increasing strain-rates and to increase with temperature decrease [51, 53]. However, opposite behavior is anticipated for the gradient term; that is, gradients are inversely proportional to the length scale over which plastic and/or damage deformations occur. Therefore, the strain-rate effect and temperature variation are crucial to the reliability of the proposed length scale parameters. Particularly, in dynamic problems their inclusion becomes more necessary. To the authors' best knowledge, very limited numerical investigations and experimental studies have been carried out that incorporate the influence of strain-rate and temperature variation on the gradient plasticity and damage, or more specifically, on the size effect. Motivated by this crucial observation, Abu Al-Rub and Voyiadjis [51] formulated the following evolution equation for the length scale parameter based on dislocation mechanics of metallic materials, such that:

$$\dot{\ell} = \ell \nu_o \exp\left[-\left(U_o / kT \right) \left\{ 1 - \left(\sigma^* / \sigma_o^* \right)^p \right\}^q \right] \tag{21}$$

where ν_o is the fundamental vibration frequency of the dislocation, p and q are material constants, k is the Boltzmann's constant, U_o is the referential activation energy, σ^* is the thermal stress, and σ_o^* is the reference thermal stress.

Voyiadjis and Abu Al-Rub [53] also formulated a length scale based on the Taylor model in dislocation mechanics, that the material length scale ℓ is identified to be in the order of the average distance between dislocations (i.e. that $\ell \propto L_S$) such that

$$\ell = \hbar L_S \qquad \text{with} \qquad \hbar = \left(\alpha_G / \alpha_S\right)^2 \left(b_G / b_S\right) \bar{M}\, \bar{r} \tag{22}$$

where L_S is the mean path of the dislocation, b_S and b_G are the magnitudes of the Burgers vectors associated with the SSDs (statistically stored dislocations) and GNDs, (geometrically necessary dislocations) respectively, α_S and α_G are statistical coefficients which account for the deviation from the regular spatial arrangements of the SSD and GND populations, respectively, $\bar{r}$ is the Nye factor ($\bar{r} \approx 2$ [54]), and $\bar{M}$ is the Schmidt's orientation factor (usually taken equal to 1/2).

Haque and Saif [55] showed that ℓ is not a fixed parameter and depends on the mean grain size d. This is in line with the dependence of the mean free path distance L_S on the plastic strain p, the hardening exponent m, and the grain size d. One, therefore, requires an evolution equation for the material length scale that is consistent with the experimental trends, such that the following expression for the length scale parameter ℓ can be adopted [53]:

$$\ell = \frac{\hbar D d}{D + d\, p^{1/m}} \tag{23}$$

Eq. (23) shows that the length scale parameter decreases with strain, increases with grain size, increases with D, and decreases with the hardening exponent. It also gives the important finding that ℓ / D decreases if the ratio D/d increases. Eq. (23) is a simple relation that gives feasible interpretations of the length scale in terms of the strain, grain size, mean number of grains through size D, and hardening as compared to the above experimental observations. Moreover, Eq. (23) shows that the intrinsic material length-scale decreases from an initial value $\ell = \hbar d$ at yield to a final value of $\ell \to 0$ at very high values of D or p (corresponds to the classical, local plasticity limit).

4.Computational aspects of the proposed theory

The development of computational algorithms that are consistent with the proposed theoretical formulation is given in detail in this paper. The problem of numerically integrating the constitutive equations in the context of the finite element method is also addressed. The standard return mapping algorithms of rate-independent problems are extended to rate-dependent problems. Moreover, since the numerical implementation of the gradient-dependent constitutive equations is not a direct task, because of the higher order of the governing equations, a direct and simple computational algorithm for the gradient approach is utilized. This algorithm can be implemented in the existing finite element code.

4.1 Numerical Integration

In any numerical scheme employed for the analysis of elasto-viscoplastic problems, it eventually becomes necessary to integrate the constitutive equations governing the material behavior. In this section, the numerical integration of the nonlocal geometrically nonlinear thermo-viscoinelatic model presented in the previous section is developed. Let t_o, t_1, … , t_n, $t_{n+1} = t_n + \Delta t$, … be convenient time instances along the time interval over which the dynamic response of the body is sought. Consider the time step $\Delta t = t_{n+1} - t_n$: at $t = t_n$ where all quantities are known, which are the converged values of the previous step, and the solution must be computed at t_{n+1} for a given body load increment, $\Delta \boldsymbol{b}$, and surface load increment, $\Delta \boldsymbol{t}$.

Let the dynamic evolution of a hypoelastic-thermo-viscoplastic and thermo-viscodamaged body of volume V and surface S be governed at time step $n+1$, by the constitutive relations presented in the previous section and by the following momentum, initial, and compatibility relations:

$$\boldsymbol{L}^T \boldsymbol{\tau}_{n+1} + \rho_o \boldsymbol{b}_{n+1} = \rho_o \dot{\boldsymbol{\upsilon}}_{n+1} \quad \text{in } V; \quad \boldsymbol{t}_{n+1} = \boldsymbol{\tau}_{n+1} \boldsymbol{n} \text{ on } S_t \tag{24}$$

$$\boldsymbol{u} = \boldsymbol{u}_o, \quad \boldsymbol{\upsilon} = \boldsymbol{\upsilon}_o \quad \text{at } t = t_o \tag{25}$$

$$\boldsymbol{l}_{n+1} = \nabla \boldsymbol{\upsilon}_{n+1} = \boldsymbol{C}\, \boldsymbol{\upsilon}_{n+1} \text{ in } V \tag{26}$$

$$\boldsymbol{u}_{n+1} = \tilde{\boldsymbol{u}} \text{ on } S_u; \quad \boldsymbol{\upsilon}_{n+1} = \tilde{\boldsymbol{\upsilon}} \text{ on } S_\upsilon; \quad T_{n+1} = \tilde{T} \text{ on } S_T \tag{27}$$

where $(\bullet)_{n+1} = (\bullet)_n + \Delta(\bullet)$ is the additive decomposition of each of the internal variables. For algorithmic convenience, the authors have shifted to matrix vector notation in this section. Eqs. (24) express the discrete dynamic motion in the volume V and equilibrium on the free part of the boundary S_t at $n+1$. Visco-hypoelasticity

is not considered in this study; viscous damping effects are neglected. $\boldsymbol{L}$ is the differential operator, $\boldsymbol{b}$ and $\boldsymbol{t}$ are the body force and the surface traction vectors, respectively, $\boldsymbol{u}$ is the three-component displacement vector, and $\boldsymbol{n}$ denotes the outward normal to the surface *S*. The initial conditions on displacements and velocities are given by Eqs. (25). Compatibility relation in volume *V* is given by Eq. (26). The boundaries S_u, S_υ, and S_T are parts of the boundary where the displacement $\tilde{\boldsymbol{u}}$, the velocity $\tilde{\boldsymbol{\upsilon}}$, and the temperature $\tilde{T}$ is prescribed, respectively. It is clear that $S_t \bigcup S_u \bigcup S_\upsilon \bigcup S_T = S$ and $S_t \bigcap S_u = \emptyset$.

In the context of the finite element method, the discrete problem can be obtained via a spatial displacement–based projection of the semidiscrete (i.e. discrete in space and continuous in time) problem into a finite dimensional subspace of admissible continuous shape functions. Consequently, in the following sections the procedure for solving the derived set of governing equations using the finite element method is described thoroughly. In order to integrate the set of constitutive equations, a return mapping algorithm is developed in the subsequent sections.

4.2. Return Mapping Algorithm

Considering a given configuration of known set of positions $\boldsymbol{X}$ at time t_n, the problem is now to update all state variables to a new configuration defined by its respective set of positions $\boldsymbol{x}$ (which are supposed to be known) at time t_{n+1}. This situation typically arises in a nonlinear finite element problem where the new positions $\boldsymbol{x}$ are determined from the discretized version of the momentum equation, Eq. (24).

In this section a semi-implicit stress integration algorithm for rate-dependent problems [56] is recalled. This stress update algorithm treats the rate-independent and rate-dependent problems in a unified way. It is unified in a sense that the same routines are able to integrate both rate-independent and rate-dependent models by simply setting the viscosity parameter, η^v, in Eqs. (8) and (9) to zero. Moreover, in this paper this algorithm is extended to fully nonlocal coupled viscoplastic-viscodamage constitutive equations with a two-step predictor-corrector structure: hypoelastic predictor and coupled viscoplastic-viscodamage corrector [57]. In the model presented in this paper, there exists two coupled surfaces, f and g, and for each iteration f and g should be corrected simultaneously (see Fig. 2). The different steps of the integration algorithm are detailed below.

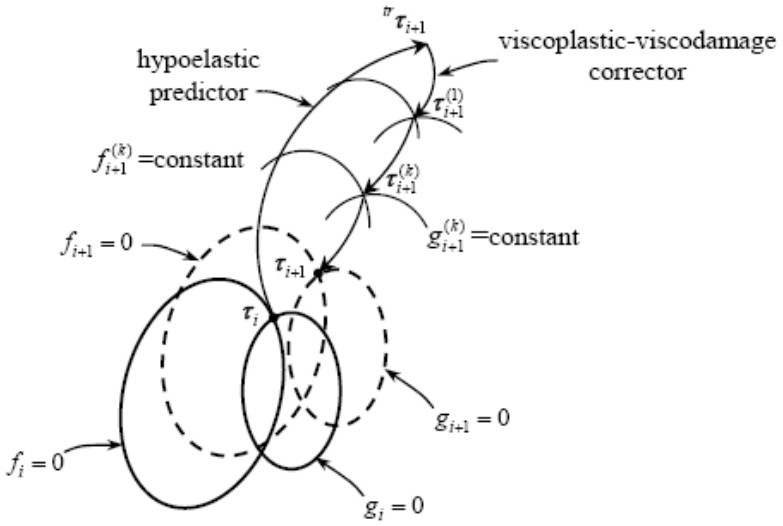

Figure 2: Conceptual representation of the hypoelastic predictor and coupled viscoplastic- viscodamage corrector algorithm [13].

If the variables at iteration i, such as $\boldsymbol{\tau}_i$, $\widehat{\boldsymbol{X}}_i$, $\widehat{R}_i$, $\widehat{\boldsymbol{\phi}}_i$, $\widehat{\boldsymbol{H}}_i$, $\widehat{K}_i$, $\widehat{\boldsymbol{Y}}_i$, and T_i, are assumed to be determined and the values of $\boldsymbol{d}$ and Δt are given, then $\boldsymbol{\tau}_{i+1}$ that satisfies the discretized constitutive equations can be obtained. In the following, a hypoelastic predictor and coupled viscoplastic-viscodamage corrector is proposed. In the first step, the hypoelastic predictor problem is solved with initial conditions that are the converged values of the previous iteration i while keeping the irreversible variables frozen. This produces a trial stress state, $\boldsymbol{\tau}^{tr}$, which, if outside the viscoplastic surface f and the viscodamage surface g is taken as the initial conditions for the solution of the viscoplastic-viscodamage corrector problem. The scope of this second step is to restore the generalized consistency condition by returning back the trial stress to the viscoplastic surface f and the viscodamage surface g simultaneously as conceptually represented in Fig. 2.

However, one of the major challenges while integrating the constitutive equations in finite deformation context is to achieve the incremental objectivity, i.e. to maintain correct rotational transformation properties all along a finite time step. A procedure that has now become very popular is first to rewrite the constitutive equations in a corotational moving frame. Therefore, Voyiadjis et al. [56] showed that by assuming that the variables of the model at iteration i and the displacement field $\boldsymbol{u}=\boldsymbol{x}_{i+1}-\boldsymbol{x}_i$ at iteration $i+1$ are known, the trial elastic stress can then be given in the corotational frame by

$$^{tr}\boldsymbol{\tau}_{i+1}=\boldsymbol{R}\left(\boldsymbol{\tau}_i+\mathbb{C}_i:\boldsymbol{E}\right)\boldsymbol{R}^T \tag{28}$$

where $\boldsymbol{R}$ is the polar decomposition ($\boldsymbol{F} = \boldsymbol{R}.\boldsymbol{U}$) rotation matrix and $\boldsymbol{E}$ is the (incremental) logarithmic strain tensor between the reference configuration and the current one, which is given by

$$\boldsymbol{E} = \ln \boldsymbol{U} = \frac{1}{2} \ln \boldsymbol{U}^2 = \frac{1}{2} \ln \left(\boldsymbol{F}^T \boldsymbol{F} \right) \tag{29}$$

In the above procedure, it is essential to realize that $\boldsymbol{F} = \boldsymbol{R}.\boldsymbol{U}$ are incremental tensors; in the case of rigid body motion, $\ln \boldsymbol{U} = \boldsymbol{0}$, thus the stress tensor will be updated exactly by the relation $\boldsymbol{\tau}_{n+1} = \boldsymbol{R} \boldsymbol{\tau}_n \boldsymbol{R}^T$ whatever the amplitude of the rotation. The rotation tensor $\boldsymbol{R}$ is directly and exactly computed from the polar decomposition and $\boldsymbol{R}$ only needs to be evaluated once per time step. All kinematic quantities are based on the deformation gradient $\boldsymbol{F}$ over the considered time step, a quantity that is readily available in nonlinear finite element codes.

4.3. Coupled Viscoplastic-Viscodamage Corrector

Now if $f\left({}^{tr}\tau_{i+1}, \widehat{\boldsymbol{X}}_i, \widehat{R}_i, \dot{\hat{p}}, T_i, \widehat{\boldsymbol{\phi}}_i \right) \le 0$ and $g\left({}^{tr}\widehat{Y}_{i+1}, \widehat{\boldsymbol{H}}_i, \widehat{K}_i, \dot{\hat{p}}_i, T_i, \widehat{\boldsymbol{\phi}}_i \right) \le 0$, the process is clearly undamaged elastic and the trial stress is in fact the final state. On the other hand, if $f > 0$ and $g > 0$, the Kuhn-Tucker loading/unloading conditions, Eqs. (10), are violated by the trial stress which now lies outside f and g (see Fig. 2). Consistency, is restored by a generalization of the classical return mapping algorithm to rate-dependent problems [56]. Since the objective rates reduce to a simple time derivative due to the fact that the global configuration is held fixed, the coupled viscoplastic-viscodamage corrector problem may then be rephrased as:

$$\dot{\boldsymbol{\tau}} = -\mathbb{C} : \left(\boldsymbol{d}^{vp} + \boldsymbol{d}^{vd} \right) - \boldsymbol{A} : \dot{\boldsymbol{\phi}} - \mathbb{C} : \alpha_t \dot{T} \boldsymbol{1} \tag{30}$$

The hypoelastic predictor and coupled viscoplastic-viscodamage corrector step yields the final stress as:

$$\boldsymbol{\tau}_{i+1} = {}^{tr}\boldsymbol{\tau}_{i+1} - \mathbb{C}_i : \left(\boldsymbol{d}^{vp} + \boldsymbol{d}^{vd} \right) - \boldsymbol{A}_i : \dot{\boldsymbol{\phi}} - \mathbb{C}_i : \alpha_t \dot{T} \boldsymbol{1} \tag{31}$$

where $\dot{T}$ is calculated from the heat balance equation, The following Lagrangian Parameters, $\dot{\lambda}^{vp}$ and $\dot{\lambda}^{vd}$ are calculated using the nonlocal computational algorithm presented in [58, 59]. In the following sequence, $\dot{\lambda}^{vp}$ and $\dot{\lambda}^{vd}$ that appear in Eqs. (7) are calculated using the nonlocal computational algorithm in [58] through the adiabatic heating condition, Eq.(19), the generalized viscoplastic consistency condition, Eq.(8), and the generalized viscodamage consistency condition, Eq. (9).

By making use of the evolution equations for $\boldsymbol{d}^{vp}$ and $\boldsymbol{d}^{vd}$ from Eqs. $(7)_1$ and $(7)_2$, respectively, into the adiabatic heat equation, Eq. (19), the temperature evolution can then be reduced to:

$$\dot{T} = \frac{1}{\rho_o c_p} J^e P \boldsymbol{1} : \boldsymbol{d} + Q_1^{tp} \dot{\lambda}^{vp} + Q_1^{td} \dot{\lambda}^{vd}, \tag{32}$$

where Q_1^{tp} and Q_1^{td} are obtained from the previous iteration i and are given by

$$Q_1^{tp} = \frac{1}{\rho_o c_p} \Upsilon \boldsymbol{\tau}' : \frac{\partial f}{\partial \boldsymbol{\tau}}, \quad Q_1^{td} = \frac{1}{\rho_o c_p} \Upsilon \boldsymbol{\tau}' : \frac{\partial f}{\partial \boldsymbol{Y}}. \tag{33}$$

Moreover, one requires the satisfaction of the generalized viscoplasticity consistency condition $\dot{f}$, Eq. (8), at the end of iteration $i+1$, such that

$$\frac{\partial f}{\partial \overline{\boldsymbol{\tau}}} : \overset{\nabla}{\overline{\boldsymbol{\tau}}} + \frac{\partial f}{\partial \overline{\overline{\boldsymbol{X}}}} : \overset{\nabla}{\overline{\overline{\boldsymbol{X}}}} + \frac{\partial f}{\partial \overline{\overline{R}}} \dot{\overline{\overline{R}}} + \frac{1}{\Delta t} \frac{\partial f}{\partial \dot{\overline{\overline{p}}}} \dot{\overline{\overline{p}}} + \frac{\partial f}{\partial T} \dot{T} = 0. \tag{34}$$

Since the local iteration process is applied within the time step $t + \Delta t$ (i.e. at step *n* + 1) and the updated Lagrangian formulation is used then $\dot{\overline{\overline{p}}} = \ddot{\overline{\overline{p}}} \Delta t$ is used in obtaining Eq.(34). Substitution of the stress rate equation, $\overset{\nabla}{\overline{\boldsymbol{\tau}}}$, from Eq. (5) and Eqs. (11), (12), and (32) into Eq. (34) yields the following expression:

$$\left(\frac{\partial f}{\partial \boldsymbol{\tau}} : \boldsymbol{C} + \mathbf{Z}^p \right) : \boldsymbol{d} + Q_1^p \dot{\lambda}^{vp} + Q_2^p \nabla^2 \dot{\lambda}^{vp} + Q_3^p \dot{\lambda}^{vd} + Q_4^p \nabla^2 \dot{\lambda}^{vd} = 0 \tag{35}$$

where $\mathbf{Z}^p$ and Q_k^p ($k = 1,...,4$) are obtained from the previous iteration i and are given by:

$$\boldsymbol{Z}^p = -\frac{\partial f}{\partial T} . \left(J^e P + T \alpha_t \right) \mathbf{1}, \tag{36}$$

$$\begin{aligned} Q_1^p = Q_1^{tp} - \frac{\partial f}{\partial \boldsymbol{\tau}} : \left(\boldsymbol{C} : \frac{\partial f}{\partial \boldsymbol{\tau}} + \boldsymbol{A} : \frac{\partial f}{\partial \boldsymbol{Y}} \right) + \left[\frac{\partial f}{\partial p} + \frac{1}{\Delta t} \frac{\partial f}{\partial \dot{p}} \right] \frac{\left(1 - k_1 \overline{\overline{R}} \right)}{1 - \hat{r}} + \\ \left[\frac{\partial f}{\partial \nabla^2 p} + \frac{1}{\Delta t} \frac{\partial f}{\partial \nabla^2 \dot{p}} \right] \times \left[\frac{\nabla^2 r}{\left(1 - \hat{r} \right)^2} \left(1 - k_1 \overline{\overline{R}} \right) - \frac{k_1}{1 - \hat{r}} \nabla^2 \overline{R} \right] - \\ \frac{1}{a_2} \frac{\partial f}{\partial \overline{\overline{\boldsymbol{X}}}} : \widehat{\boldsymbol{M}} : \left(\frac{\partial f}{\partial \overline{\overline{\boldsymbol{X}}}} + k_2 \overline{\overline{\boldsymbol{X}}} \right) - \frac{2}{a_2 \ell^2} \frac{\partial f}{\partial \nabla^2 \overline{\overline{\boldsymbol{X}}}} : \\ \left[\nabla^2 \widehat{\boldsymbol{M}} : \left(\frac{\partial f}{\partial \overline{\overline{\boldsymbol{X}}}} + k_2 \overline{\overline{\boldsymbol{X}}} \right) + k_2 \widehat{\boldsymbol{M}} : \nabla^2 \overline{\overline{\boldsymbol{X}}} \right] + \frac{\partial f}{\partial \boldsymbol{\phi}} : \frac{\partial f}{\partial \boldsymbol{Y}} \end{aligned} \tag{37}$$

$$\begin{aligned} Q_2^p = \left[\frac{\partial f}{\partial \nabla^2 p} + \frac{1}{\Delta t} \frac{\partial f}{\partial \nabla^2 \dot{p}} \right] \frac{\left(1 - k_1 \overline{\overline{R}} \right)}{1 - \hat{r}} - \frac{2}{a_2 \ell^2} \frac{\partial f}{\partial \nabla^2 \overline{\overline{\boldsymbol{X}}}} : \widehat{\boldsymbol{M}} : \left(\frac{\partial f}{\partial \overline{\overline{\boldsymbol{X}}}} + k_2 \overline{\overline{\boldsymbol{X}}} \right) + \\ \frac{\partial f}{\partial \nabla^2 \boldsymbol{\phi}} : \frac{\partial f}{\partial \boldsymbol{Y}} \end{aligned} \tag{38}$$

$$Q_3^p = Q_1^{td} - \frac{\partial f}{\partial \boldsymbol{\tau}} : \left(\boldsymbol{C} : \frac{\partial g}{\partial \boldsymbol{\tau}} + \boldsymbol{A} : \frac{\partial g}{\partial \boldsymbol{Y}} \right) + \frac{\partial f}{\partial \boldsymbol{\phi}} : \frac{\partial g}{\partial \boldsymbol{Y}} , \tag{39}$$

$$Q_4^p = \frac{\partial f}{\partial \nabla^2 \boldsymbol{\phi}} : \frac{\partial g}{\partial \boldsymbol{Y}} . \tag{40}$$

Similarly, the generalized viscodamage consistency condition $\dot{g}$, Eq. (9), needs to be satisfied. Since the viscodamage driving forces $\widehat{\boldsymbol{Y}}$ is a function of $\boldsymbol{\tau}$ and $\widehat{\boldsymbol{\phi}}$ one can then express $\dot{g}$ as follows:

$$\dot{g} \equiv \frac{\partial g}{\partial \boldsymbol{\tau}} : \overset{\triangledown}{\boldsymbol{\tau}} + \frac{\partial g}{\partial \widehat{\boldsymbol{\phi}}} : \overset{\triangledown}{\widehat{\boldsymbol{\phi}}} + \frac{\partial g}{\partial \widehat{\boldsymbol{H}}} : \overset{\triangledown}{\widehat{\boldsymbol{H}}} + \frac{\partial g}{\partial \widehat{K}} \dot{\widehat{K}} + \frac{1}{\Delta t} \frac{\partial f}{\partial \dot{\bar{p}}} \dot{\bar{p}} + \frac{\partial g}{\partial T} \dot{T} = 0 \tag{41}$$

Substitution of the stress rate equation, $\overset{\triangledown}{\boldsymbol{\tau}}$, from Eq. (2) along with Eqs. (7), (13), (14), and (32) into Eq. (41) yields the following expression:

$$\left(\frac{\partial g}{\partial \boldsymbol{\tau}} : \boldsymbol{C} + \mathbf{Z}^d \right) : \boldsymbol{d} + Q_1^d \dot{\lambda}^{vp} + Q_2^d \nabla^2 \dot{\lambda}^{vp} + Q_3^d \dot{\lambda}^{vd} + Q_4^d \nabla^2 \dot{\lambda}^{vd} = 0 , \tag{42}$$

where $\mathbf{Z}^d$ and Q_k^d ($k = 1,...,4$) are obtained from the previous i iteration and are given by:

$$\mathbf{Z}^d = -\left(\frac{\partial g}{\partial T} - \frac{\partial g}{\partial \boldsymbol{\tau}} : \alpha_t \mathbf{1} \right) . \left(J^e P + T \alpha_t \right) \mathbf{1} , \tag{43}$$

$$Q_1^d = Q_1^{tp} - \frac{\partial g}{\partial \boldsymbol{\tau}} : \left(\boldsymbol{C} : \frac{\partial f}{\partial \boldsymbol{\tau}} + \boldsymbol{A} : \frac{\partial f}{\partial \boldsymbol{Y}} \right) + \frac{\partial g}{\partial \boldsymbol{\phi}} : \frac{\partial f}{\partial \boldsymbol{Y}} , \tag{44}$$

$$Q_2^d = \frac{\partial g}{\partial \nabla^2 \boldsymbol{\phi}} : \frac{\partial f}{\partial \boldsymbol{Y}} , \tag{45}$$

$$\begin{aligned} Q_3^d = Q_1^{td} &- \frac{\partial g}{\partial \boldsymbol{\tau}} : \left(\boldsymbol{C} : \frac{\partial g}{\partial \boldsymbol{\tau}} + \boldsymbol{A} : \frac{\partial g}{\partial \boldsymbol{Y}} \right) + \frac{\partial g}{\partial r} \left(1 - h_1 \widehat{K} \right) - \frac{2 h_1}{a_3 \ell^2} \frac{\partial g}{\partial \nabla^2 r} \nabla^2 K + \frac{1}{\Delta t} \frac{\partial g}{\partial \dot{\bar{p}}} \\ &- \frac{1}{a_4} \frac{\partial g}{\partial \boldsymbol{H}} : \left(\frac{\partial g}{\partial \boldsymbol{H}} + h_2 \widehat{\boldsymbol{H}} \right) - \frac{2 h_2}{a_4 \ell^2} \frac{\partial g}{\partial \nabla^2 \boldsymbol{H}} : \nabla^2 \boldsymbol{H} + \frac{\partial g}{\partial \boldsymbol{\phi}} : \frac{\partial g}{\partial \boldsymbol{Y}} , \end{aligned} \tag{46}$$

$$Q_4^d = \frac{\partial g}{\partial \nabla^2 r} \left(1 - h_1 \widehat{K} \right) + \frac{1}{\Delta t} \frac{\partial g}{\partial \nabla^2 \dot{\bar{p}}} - \frac{2 h_2}{a_4 \ell^2} \frac{\partial g}{\partial \nabla^2 \boldsymbol{H}} \left(\frac{\partial g}{\partial \boldsymbol{H}} + h_2 \widehat{\boldsymbol{H}} \right) + \frac{\partial g}{\partial \nabla^2 \boldsymbol{\phi}} \Bigg|^T \frac{\partial g}{\partial \boldsymbol{Y}} . \tag{47}$$

Due to the higher order of the governing equations, Eqs. (35) and (42), in the inelastic region, considerable difficulties are experienced with their numerical implementation. The consistency condition of inelasticity is no longer an algebraic equation but is a differential one because of $\nabla^2 \dot{\lambda}^{vp}$ and $\nabla^2 \dot{\lambda}^{vd}$, which needs to be calculated along with $\dot{\lambda}^{vp}$ and $\dot{\lambda}^{vd}$. Another complication is the higher-order boundary conditions that are necessary from the mathematical point of view and have to be prescribed on the moving elasto-inelastic boundary (Fig. 3). These internal boundaries are not always easy to interpret physically. In the following, the robust numerical technique that have been developed in [58,59] is used to calculate the Laplacian terms $\nabla^2 \dot{\lambda}^{vp}$ and $\nabla^2 \dot{\lambda}^{vd}$.

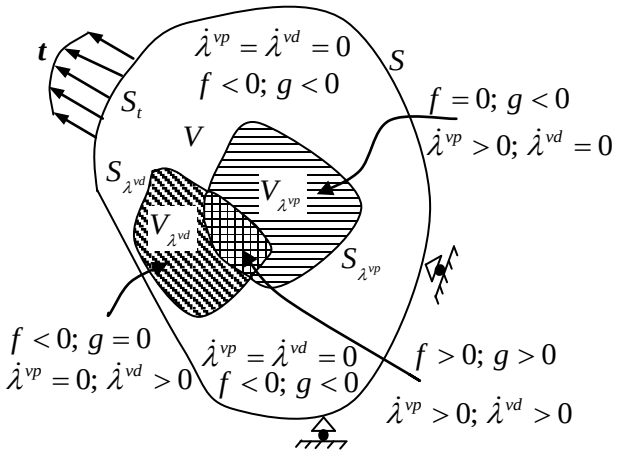

Fig. 3: Schematic representation of elastic, viscoplastic, and viscodamage boundaries [13].

5.Numerical Applications

Several numerical examples are presented in this chapter in order to validate and test the proposed computational framework and numerical algorithm using the proposed coupled nonlocal viscoplastic damage model. This is accomplished by implementation of the current constitutive microdamage model and the proposed numerical integration algorithm in the explicit commercial finite element code ABAQUS/Explicit [60] using the user material subroutine VUMAT.

5.1 Example1: Shear localizations in strip tension

In the first example of this section, local viscoplastic fromulation is considered only for a shear localization problem in order to study the adiabatic shear band localizations in tensile deformation for several bcc metals [61, 62].

A simple uniaxial plane strain tension problem, with 10mm x 20mm dimensions as shown in Figure 4, is considered in this case. The theoretical formulations and computational algorithms of the proposed elasto-viscoplastic constitutive models are tested by studying the mesh sensitivity problem using different mesh configurations. In this regard, the considered problem is modeled and meshed with five different mesh discretizations (Mesh1: 10×20, Mesh2: 15×30, Mesh3: 20×40, Mesh4: 25×30, Mesh5: 30×60 elements) using the four-node plane strain element with reduced integration.

In this example, the differences between the rate-independent and rate-dependent plasticity constitutive equations was investigated by applying constant velocities at certain initial temperatures using the five considered meshes. For this type of problem, shear bands may be developed and formed in different directions as there is no specific imperfection or defects induced in the sample. Deformations of a homogenous body with uniform initial conditions become inhomogeneous because of the interaction with the incident waves reflected from the boundaries and corner. This may happen at different instants in the considered metals due to the differences

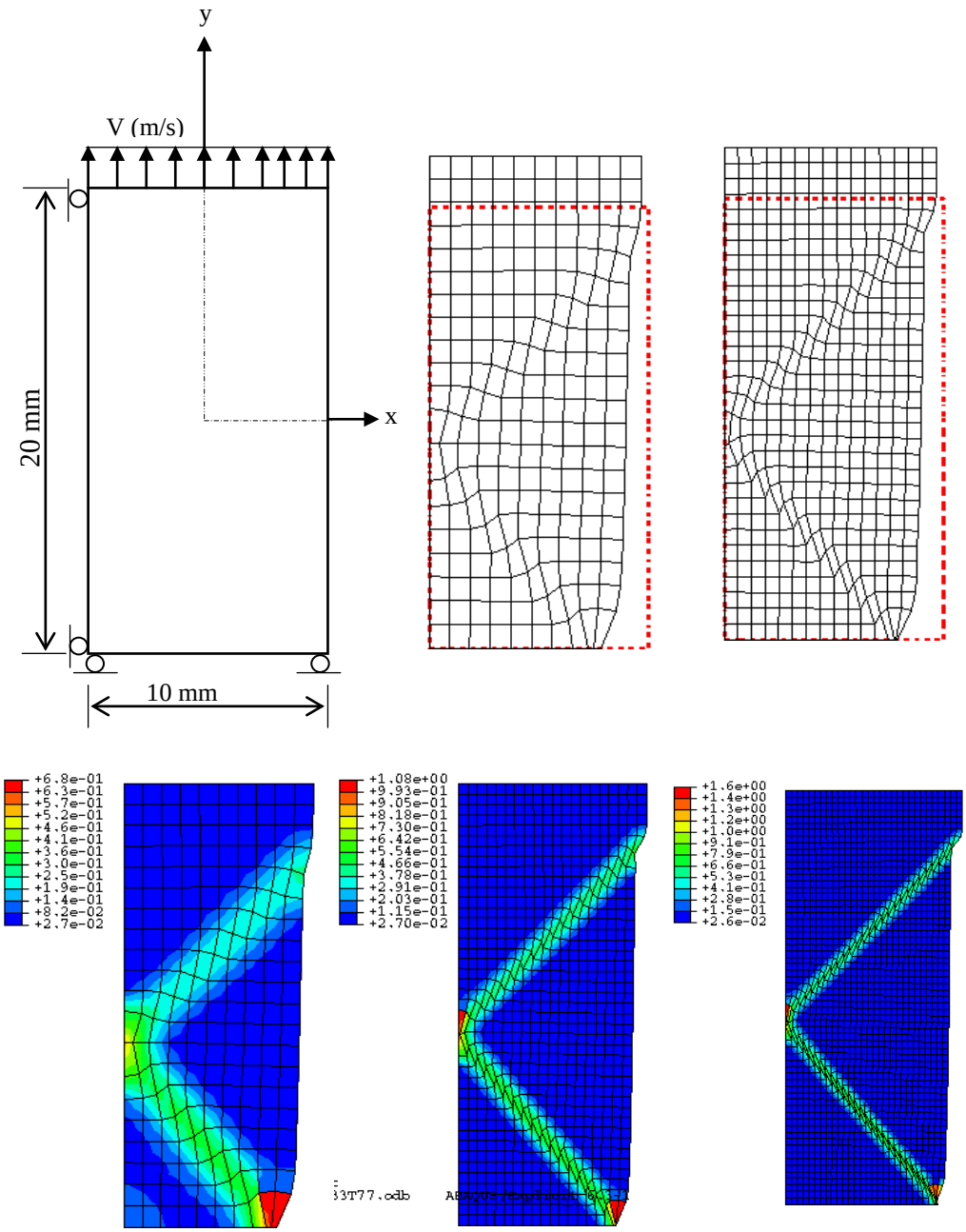

Figure 4: Illustration for a specimen subjected to certain velocity with a specified boundary condition and deformed (solid lines) and undeformed (dashed lines) patterns at 70μs time step (2.1mm elongation) [62].

in their material properties. Moreover, it may also encounter at different instants within the same metal if different velocities (different waves) are considered. However, this problem should not be affected by the mesh refinement. (i.e., by using different mesh configurations).

It is obvious from these patterns that the observed width of shear bands is determined by the element size such that the deformation is localized along a line of integration points. The von Mises stresses at the localized regions over the total elongation of the specimen (3.3mm) clearly show the mesh dependency of the considered rate-independent analysis as shown in Fig. 5.

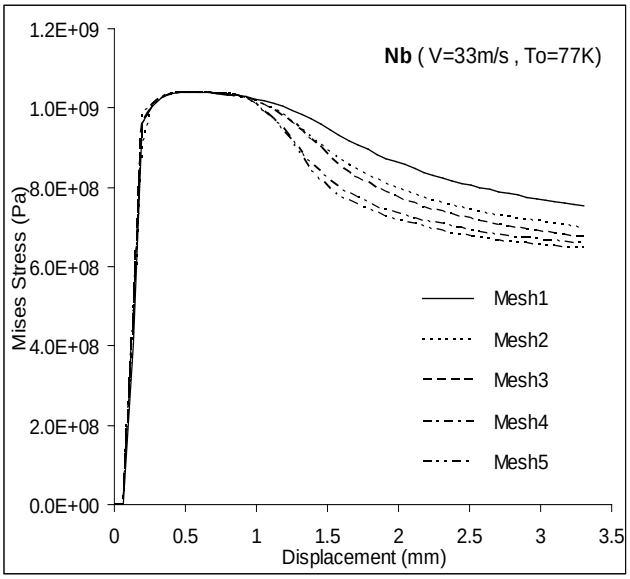

Figure 5: Mesh-dependent results for niobium using the Mises-displacement curves [62].

In order to show that the rate dependent model also regularizes nonlocal problems with an internal length scale [62] and provides mesh independent results the proposed viscoplastic model was used by applying the velocity (V=33m/s) and initial temperature (77K) over a total time step of 100μs (3.3mm total displacement) using three mesh discretizations (Mesh1, Mesh2, and Mesh3). The corresponding deformed displacement patterns are illustrated in Figure 6(a) at a time step of 83μs (2.7mm displacement). The stress (Mises)-displacement curves over the total time step is also plotted in Figure 6(b). Comparing with the results obtained from the rate-independent analysis, one observes a finite width of shear bands that is independent of the finite element size, no mesh dependence. Moreover, the Mises-displacement curves (Figure 6(b)) show almost identical results for all of the considered meshes as compared to those obtained for the rate-independent analysis.

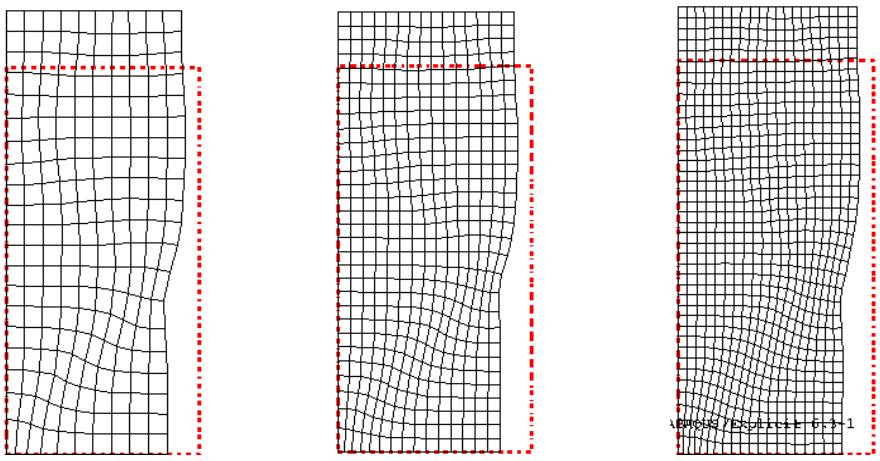

(a)

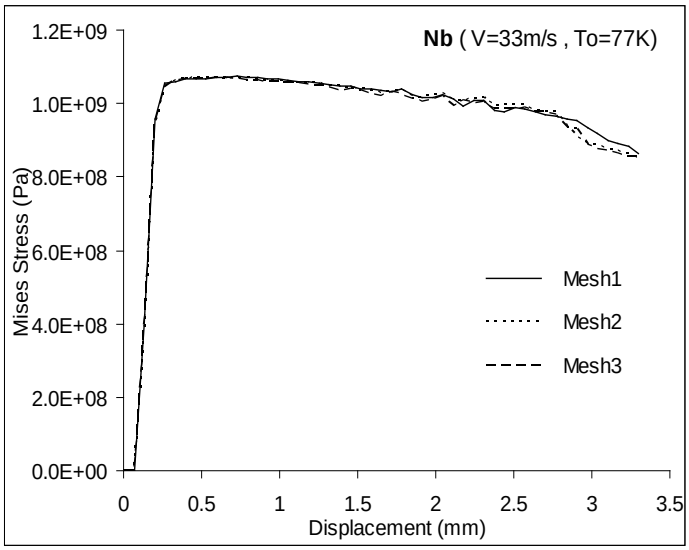

(b)

Figure 6: Mesh-independent results for niobium at V=33m/s ($1650s^{-1}$ strain rate) and To=77K. (a) Deformed (solid lines) and undeformed (dashed lines) patterns at 83μs time step (2.7mm elongation). (b) Mises-displacement curves [62].

5.2 Example 2: Shear localizations in cylindrical hat-shaped samples and comparisons with experimental results

Numerical simulations of the dynamic deformation response of tantalum hat-shaped specimens, shown schematically in Fig, 7, are performed in this study under prescribed conditions. Comparisons of these results to experiments conducted by three different authors [63-65] are also made. The hat-shaped sample geometry is commonly used to study shear localization growth. The shape indicates an axi-symmetric condition with a shear zone limited between the upper (hat) and lower (brim) portions. The proposed finite element simulations of the proposed samples assume axi-symmetry condition in which a four-node axi-symmetric type of elements is used for the problem mesh geometry.

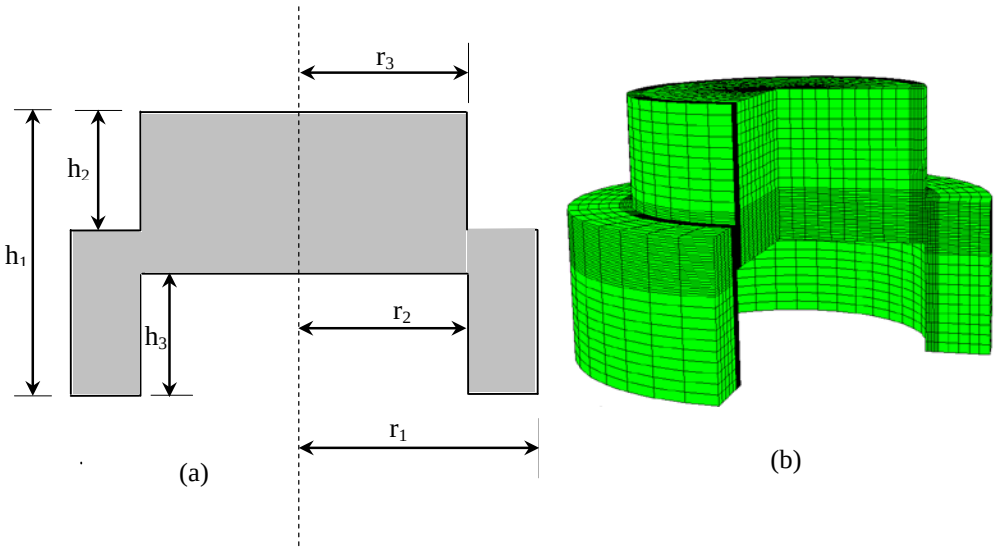

Figure 7: Cylindrical hat-shaped specimen. (a) A schematic diagram (dimensions given in Table 1). (b) A three-dimensional shape corresponding to 3/4 of the sample [62].

The finite element simulations of the above-mentioned hat-shaped sample, subjected to compressive loading at the ambient initial temperatures and three different strain rates (for the three different authors), are performed. Results for the adiabatic shear stress versus displacement of the three considered mesh density simulations compared with corresponding experimental data are given in Fig. 8.

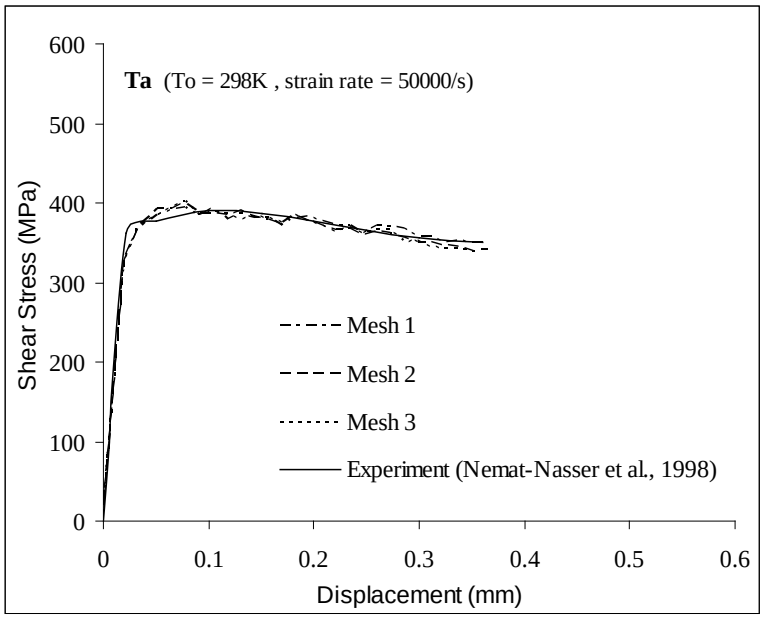

Figure 8: Shear stress vs displacement curves for tantalum under adiabatic condition. Comparison between experiment [63] and simulation results using three different mesh configurations [62].

In addition to the good comparisons between the results from simulations and experiments, it is interesting to also note that the stress-displacement curves of the adiabatically tested specimen and model simulations share a common feature, that is, the shear stress first reaches a peak value, and then decreases with increasing displacement. Simulation results of the equivalent plastic strain contours for the tantalum adiabatic simulation at the end of the considered displacement is shown in Fig. 9(a). Shear localization corresponding to pure tantalum deformed at the above mentioned loading condition compares well with the optical micrographs taken at the forced localized shear region as illustrated in Fig. 9(b). The width of the shear region increases with increasing shear strain within a given specimen.

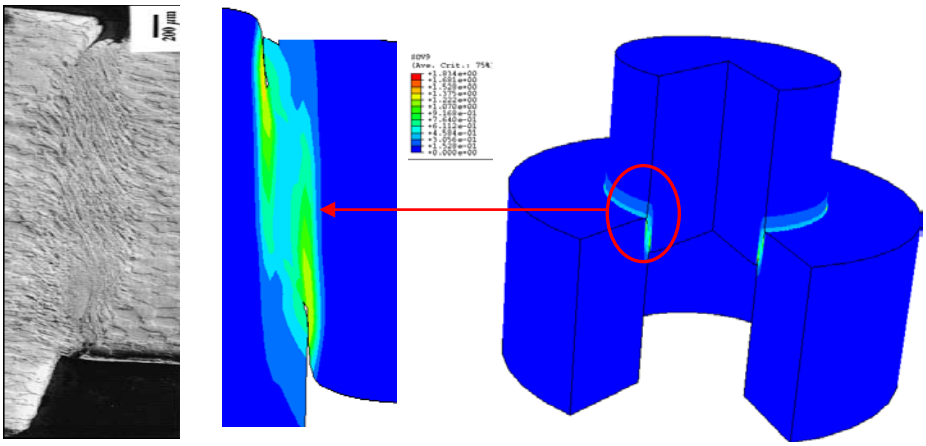

(a) (b)

Figure 9: (a) Shear localization results from experimental observations (66Perez-Prado et al., 2001) and model simulation. (b) Contour plots [64].

5.3 Example 3: simulation of the a blunt projectile impacting a target

The objective of this numerical example is to investigate if the proposed constitutive equations are able to describe the structural response to projectile impact damage when different failure modes are expected to occur. This is done by conducting numerical simulations of the experimental tests presented by Borvik et al. [9] for a blunt projectile made of hardened Arne tool steel impacting a circular plate made of Weldox 460 E steel. The model material constants of the target material of Weldox 460 E steel and for the projectile material of hardened Arne tool steel are listed in Table 1.

TABLE 1: Material constants of the target material of Weldox 460 E steel and for the projectile material of hardened Arne tool steel[13]

Target Material of Weldox 460 E steel			
$E = 200\,GPa$	$a_1 = 400\,MPa$	$h_1 = 0$	$r_0 = 0$
$\nu = 0.33$	$a_2 = 20\,GPa$	$h_2 = 0$	$\gamma = 1.7$
$\bar{Y}_o = 490\,MPa$	$a_3 = 0$	$\Upsilon = 0.9$	$m = 0.94$
$T_r = 295\,K$	$a_4 = 0$	$\ell = 5\,\mu m$	$n = 1$
$T_m = 1800\,K$	$k_1 = 0.1 MPa^{-1}$	$\alpha_t = 1.1\times10^{-5}/K$	$\phi_{eq}^c = 0.30$
$\rho_o = 7850\,kg/m^3$	$k_2 = 15\,GPa^{-1}$	$c_p = 452\,J/kg.K$	$P_{cutoff} = 160\,GPa$
$\eta^v = 0.01\,s$	$\eta_r = 0$	$c_v = 266\,J/kg.K$	
Projectile Material of Hardened Arne Tool Steel			
$E = 204\,GPa$	$\nu = 0.33$	$\rho_o = 7850\,kg/m^3$	$Y_o = 1900\,MPa$
$E_t = 15\,GPa$	$\varepsilon_f = 2.15\%$		

In these simulations a 4-node 2D axisymmetric element with one integration point and a stiffness based on hourglass control is used. Plot of the initial configuration, showing a part of the target plate and the blunt projectile just prior to impact, is shown in Fig. 10.

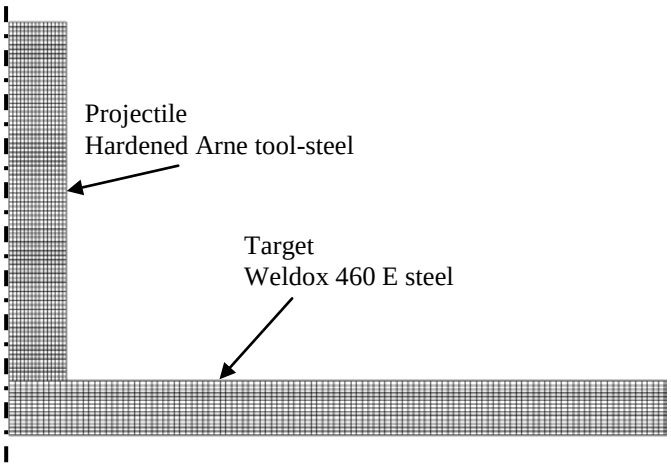

Figure 10: Finite element mesh plot of the axisymmetic initial configuration just before impact [13].

The target plate has a nominal thickness of 12mm and a diameter of 500mm, while the nominal length and diameter of the hardened projectile are 80mm and 20mm, respectively. In each run, the target plate is fully clamped at the support,

while the projectile is given an initial velocity similar to the one used in the corresponding experiment conducted by Borvik et al. [9]. In order to reduce the computational time, which is affected both by the element size and number, the mesh was somewhat coarsened towards the boundary. Owing to this coarsening the total number of elements in the target plate is less than about 10,000 in the simulations. Contact was modeled using an automatic 2D single surface penalty formulation available in ABAQUS/Explicit [60]. A friction coefficient of 0.05 is assumed between the projectile and the target. Time increments of order 10^{-8} *s* are used to satisfy the stability criteria.

Borvik et al. [66] simulations indicate the problem involving shear localization and plugging for blunt projectiles to be mesh size sensitive. However, the numerical solution using the present model is mesh size independent and converges monotonically towards a limit solution when the number of elements over the target thickness becomes sufficiently large. Therefore, the numerical results improve as the element size is reduced until it stabilizes at some value; i.e. the mesh size dependency is not pathological. This is expected since the width of the shear band is known to be in the order of 10-100 μm [67]. A direct comparison between the numerical and experimental residual velocity curves for blunt projectile is shown in Fig. 11.

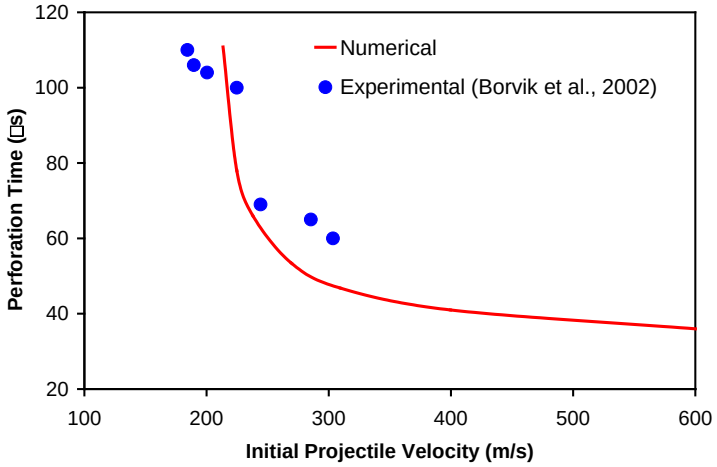

Figure 11: A comparison between numerical and experimental results by a blunt projectile for the initial impact velocity versus residual projectile velocity [13].

It is noteworthy that in Fig. 11 one cannot simply obtain the perforation time by knowing the initial and residual velocities of the projectile and the target thickness. For example, for 303.5m/s impact velocity the residual velocity from Fig. 10 is 199.7m/s. By linear kinematics and knowing that the target thickness is 12mm, one can simply calculate the perforation time to be 116 μs , whereas experimentally it is reported as 60 μs which deviates from the calculated one.

High-speed camera images showing perforation of the target plate at impact velocities close to the ballistic limit are shown in Fig. 12.

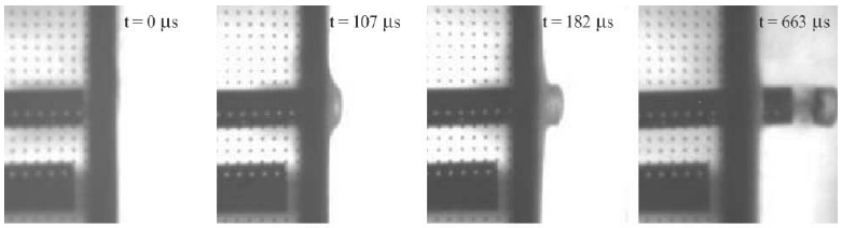

Figure 12: High-speed camera images showing perforation of the target plate at impact velocities close to the ballistic limits with a blunt projectile; after Borvik et al. [9].

Numerical plots showing perforation of the target plate by a blunt projectile at impact velocity close to the ballistic limit of 210m/s are shown in Fig. 13. The contours of accumulated viscoinelastic strain are plotted on the deformed mesh. It can be seen that limited inelastic deformation occurs outside the localized shear zone. These plots clearly demonstrate that the numerical model qualitatively captures the overall physical behavior of the target during penetration and perforation. Notice also that in these plots, only a part of the complete target plate is shown.

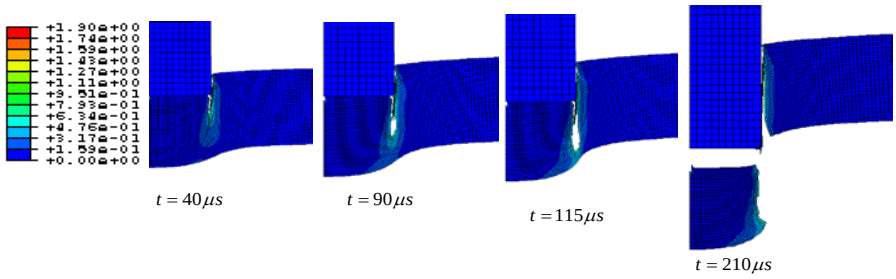

Figure 13: Perforation of the target plate by a blunt projectile of initial impact velocity of 210 m/s plotted as contours of accumulated inelastic strain and at different times. The green region indicates an accumulated damage between 0.25 and 0.30 [13].

5.4 Example 4: simulation of the a projectile impacting a composite plate

The proposed model is used to simulate a hemispherically tipped cylindrical steel projectile, 5.5mm long and 7.5mm diameter, impacting and penetrating into a 50x50x5mm laminated metal matrix composite plate subjected to an initial velocity of 1000m/s. Table 2 shows the geometrical dimensions and material parameters that are used for the projectile.

TABLE 2: Material and dimensional properties of the projectile[39].

Material Properties	Youngs's modulus, E : 210 E 9Pa Poisson ratio: 0 .28 Density : 7850kg/m^3
Dimensions of the projectile	Radius : 7.5mm Length: 5.5mm

Numerical analysis of the impact stage provides considerable kinetics and kinematic information of the penetration and perforation processes. Generally, strong shock wave-material interaction is generated and propagated along both the projectile and the targets that can lead to fracture global inelastic strains. Phenomenologically, the penetration can be viewed as a process to generate a cone shaped macrocrack in the material, in which the kinetic energy of the penetrator is dissipated. In Fig. 14 the sequence of stages of impact can be seen.

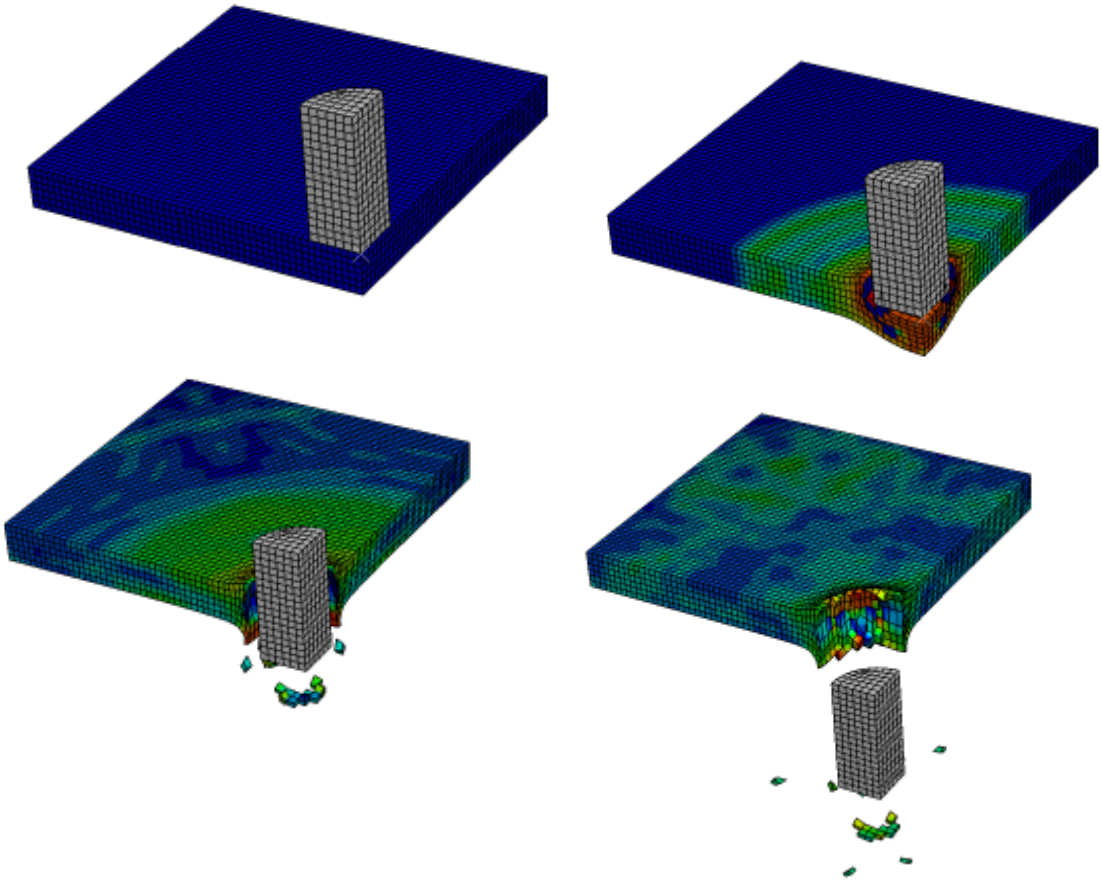

Figure 14: Deformation stages of the plate during the impact process [39].

Global bending and dishing is observed in the third stage. Numerical plots of the perforation of the target plate by the projectile shows the limited inelastic deformation that occurs outside of the localized shear zone. These plots clearly indicate that the numerical model qualitatively captures the overall physical behavior of the target during penetration and perforation. In the third and fourth stages of deformation of the plate (a and b) it can be seen that the elements in the impacted area are significantly distorted. However, stable results are nevertheless obtained. This distortion caused delay in the damage evolution process and, consequently the erosion of the failed elements. This simulation also indicates that the initiation and propagation of the microdefects depend on both the amplitude and distribution of the inelastic strain/stress in the vicinity around the microdefects. This implies that the evolution of the material inelasticity is practically a nonlocal process. Hence, such nonlocality in the material response requires such a micromechanical approach that incorporates material length scale parameter into the classical constitutive relations.

6.Conclusions

In this chapter a coupled rate-dependent plasticity and damage model, that were developed by Voyiadjis and Co-workers [39,40,61,62] for the last ten years, is presented. This theory were developed based on the thermodynamic consistency of the gradient-dependent plasticity/damage constitutive relations on the continuum level in order to bridge the gap between the micromechanical and classical continuum inelasticity. Implicit and explicit incorporation of material length scales is achieved through the development of coupled viscoinelasticity (rate-dependent plasticity/damage) and gradient-dependent (nonlocal) constitutive relations, respectively. Therefore, the resulting model incorporates in a very modular fashion the damage and plasticity effects in solids, and most importantly in a physically based and motivated approach.

Computational aspects of the proposed model are addressed through the finite element implementation in the finite element code (ABAQUS) with an implicit stress integration algorithm. The radial return algorithm which is a special case of the backward-Euler method is used to introduce a nonlinear scalar equation in terms of the viscoplastic multiplier for the case of the consistency in the viscoplastic model. The proposed algorithms are extensions of the classical radial return scheme for rate-independent (plasticity) problems to rate-dependent (viscoplasticity) problems**.** Namely an operator split structure consisting of a trial state followed by the return map is developed by imposing a generalized (rate-independent to rate-dependent) viscoplastic and viscodamage consistency conditions simultaneously. This allows one to integrate both rate-dependent and rate-independent models in a similar fashion. Moreover, a simple and direct computational algorithm is also used for the calculation of the Laplacian gradients

allowing one to integrate both the gradient-dependent and gradient-independent models in a similar way. Furthermore, a trivially incrementally objective integration scheme is proposed. Moreover, a simple and direct computational algorithm is also used for the calculation of the Laplacian gradients allowing one to integrate both the gradient-dependent and gradient-independent models in a similar way. The nonlinear algebraic system of equations is solved by consistent linearization and the use of the Newton–Raphson iteration. The numerical implementation then involves a series of coupled routines providing the stresses and updates of the corresponding internal variables.

Several numerical examples are presented in this chapter in order to validate and test the proposed computational framework and numerical algorithm using the proposed coupled nonlocal viscoplastic damage model. In this regard first, experimental comparisons of the adiabatic shear localizations between the proposed model simulations and other independent results are presented. Effect of initial temperatures and loading rates on the development of shear localizations is also investigated. Subsequently, shear localizations in cylindrical hat-shaped samples was investigated and comparisons with experimental results were presented. Model capabilities were preliminarily illustrated for the dynamic localization of inelastic flow in adiabatic shear bands and compared with the experimental results of Borvik et al. [9] for the perforation of 12mm thick Weldox 460E steel plates by deformable blunt projectiles at various impact speeds. Finally numerical simulations were also performed in order to investigate penetration and perforation of a projectile impacting a metal matrix composite plate.

7. REFERENCES

[1] Zukas, J. A., "High Velocity Impact Dynamics," John Wiley & Sons, Inc., New York, 1990

[2] Johnson, G. R., and Cook H. W. "Fracture Characteristics of Three Metals Subjected to Various Strains, Strain Rates, Temperature and Pressures," *Engineering Fracture Mechanics*, Vol. 21, No. 1, 1985, pp. 31-48.

[3] Curran, D. R., Seaman, L., and Shockey, D. A. "Dynamic Failure of Solids," *Physics Reports*, Vol. 147, 1987, pp. 253-388.

[4] Steinberg, D. J., and Lund, C. M. "A Constitutive Model for Strain Rates from 10^{-4} to 10^{6} /s," *Journal of Applied Physics*, Vol. 65, No. 4, 1989, pp. 1528-1533.

[5] Zerilli, F. J., and Armstrong, R. W. "Dislocation-Mechanics-Based Constitutive Relations for Material Dynamics Calculations," *Journal of Applied Physics*, Vol. 61, No. 5, 1987, pp. 445-459.

[6] Bammann, D. J, Chiesa, M. L., McDonald, A., Kawahara, W. A., Dike, J. J., and Revelli, V. D "Prediction of Ductile Failure in Metal Structures," AMD, Vol. 107, 1990, pp. 7-12.

[7] Camacho, G. T., and Ortiz, M., "Adaptive Lagrangian Modeling of Ballistic Penetration of Metallic Targets," *Int. J. Comp. Meth. Appl. Mech. Engng.*, Vol. 142, 1997, pp. 269-301.
[8] Borvik, T., Langseth, M., Hopperstad, O. S., and Malo, K. A. "Perforation of 12mm Thick Steel Plates by 20mm Diameter Projectiles with Flat, Hemispherical and Conical Noses - Part I: Experimental Study," *International Journal of Impact Engineering*, Vol. 27, No. 1, 2002, pp. 19-35.
[9] Borvik, T., Clausen, A. H., Hopperstad, O. S., and Langseth, M. "Perforation of AA5083-H116 Aluminum Plates with Conical-Nose Steel Projectiles-Experimental," *International Journal of Impact Engineering*, Vol. 30, 2004, pp. 367-384.
[10] Eftis, J., Carrasco, C., and Osegueda, R.A. "A Constitutive-Microdamage Model to Simulate Hypervelocity Projectile-Target Impact, Material Damage and Fracture," *International Journal of Plasticity*, Vol. 19, 2003, pp. 1321-1354.
[11] Voyiadjis, G. Z., and Abed, F. H. "Microstructural Based Models for BCC and FCC Metals with Temperature and Strain Rate Dependency," *Mechanics of Materials*, Vol. 37, 2005, pp. 355–378.
[12] Gonzalez, C., A. Martin, and J. Llorca, *Effect of temperature on the fracture mechanisms of 8090 Al-Li alloy and 8090 Al-Li/SiC composite.* Scripta Materialia, 2004. **51**(11): p. 1111-1115.
[13] Voyiadjis, G.Z., R.K.A. Al-Rub, and A.N. Palazotto, *Constitutive modeling and simulation of perforation of targets by projectiles.* AIAA Journal, 2008. **46**(2): p. 304-316.
[14] He, T., H.M. Wen, and Y. Qin, *Finite element analysis to predict penetration and perforation of thick FRP laminates struck by projectiles.* International Journal of Impact Engineering, 2008. **35**(1): p. 27-36.
[15] He, T., H.M. Wen, and Y. Qin, *Penetration and perforation of FRP laminates struck transversely by conical-nosed projectiles.* Composite Structures, 2007. **81**(2): p. 243-252.
[16] Bazant, Z.P., et al., *Fracturing rate effect and creep in microplane model for dynamics.* Journal of Engineering Mechanics-Asce, 2000. **126**(9): p. 962-970.
[17] Caner, F.C., et al., *Hyperelastic anisotropic microplane constitutive model for annulus fibrosus.* Journal of Biomechanical Engineering-Transactions of the Asme, 2007. **129**(5): p. 632-641.
[18] Reddy, T.Y., et al., *Penetration and perforation of composite sandwich panels by hemispherical and conical projectiles.* Journal of Pressure Vessel Technology-Transactions of the Asme, 1998. **120**(2): p. 186-194.
[19] Wen, H.M., *Predicting the penetration and perforation of targets struck by projectiles at normal incidence.* Mechanics of Structures and Machines, 2002. **30**(4): p. 543-577.
[20] Wen, H.M., *Predicting the penetration and perforation of FRP laminates struck normally by projectiles with different nose shapes.* Composite Structures, 2000. **49**(3): p. 321-329.
[21] Zukas, J.A. and D.R. Scheffler, *Impact effects in multilayered plates.* International Journal of Solids and Structures, 2001. **38**(19): p. 3321-3328.

[22] Arias, A., J.A. Rodriguez-Martinez, and A. Rusinek, *Numerical simulations of impact behaviour of thin steel plates subjected to cylindrical, conical and hemispherical non-deformable projectiles.* Engineering Fracture Mechanics, 2008. **75**(6): p. 1635-1656.
[23] Rusinek, A., et al., *Influence of conical projectile diameter on perpendicular impact of thin steel plate.* Engineering Fracture Mechanics, 2008. **75**(10): p. 2946-2967.
[24] Steinberg, D.J., S.G. Cochran, and M.W. Guinan, *A Constitutive Model for Metals Applicable at High-Strain Rate.* Journal of Applied Physics, 1980. **51**(3): p. 1498-1504.
[25] Steinberg, D.J. and C.M. Lund, *A Constitutive Model for Strain Rates from 10-4 to 106 S-1.* Journal De Physique, 1988. **49**(C-3): p. 433-440.
[26] Steinberg, D.J. and C.M. Lund, *A Constitutive Model for Strain Rates from 10-4 to 106 S-1.* Journal of Applied Physics, 1989. **65**(4): p. 1528-1533.
[27] Preston, D.L., D.L. Tonks, and D.C. Wallace, *Model of plastic deformation for extreme loading conditions.* Journal of Applied Physics, 2003. **93**(1): p. 211-220.
[28] Matzenmiller, A., J. Lubliner, and R.L. Taylor, *A Constitutive Model for Anisotropic Damage in Fiber-Composites.* Mechanics of Materials, 1995. **20**(2): p. 125-152.
[29] Arevalo, E., et al., *Modeling low velocity impact in C/Epoxy laminates*, in *23th International symposium on balistics*. 2007: Tarragona, Spain p. 1123-1126.
[30] Ji., C., et al., *Impact Damage of 3D Orthogonal Wowen Compoiste Circular Plates.* Appl. Compos. Mater., 2007. **14**: p. 343-362.
[31] Lee, W.S., C.H.R. Lai, and S.T. Chiou, *Numerical study on perforation behavior of 6061-T6 aluminum matrix composite.* Journal of Materials Processing Technology, 2001. **117**(1-2): p. 125-131.
[32] Chang, F.K. and K.Y. Chang, *A Progressive Damage Model for Laminated Composites Containing Stress-Concentrations.* Journal of Composite Materials, 1987. **21**(9): p. 834-855.
[33] Kumar, K.S. and T.B. Bhat, *Response of composite laminates on impact of high velocity projectiles.* Impact Response and Dynamic Failure of Composites and Laminate Materials, Pts 1 and 2, 1998. **141-1**: p. 337-348.
[34] Kumar, S., B.N. Rao, and B. Pradhan, *Effect of impactor parameters and laminate characteristics on impact response and damage in curved composite laminates.* Journal of Reinforced Plastics and Composites, 2007. **26**(13): p. 1273-1290.
[35] Banerjee, B., *An evaluation of plastic flow stress models for the simlation of high-temperature and high strain-rate deformation of metals*. 2005.
[36] Voyiadjis, G. Z., Abu Al-Rub, R. K., and Palazotto, A. N. "Non-Local Coupling of Viscoplasticity and Anisotropic Viscodamage for Impact Problems Using the Gradient Theory," *Archives of Mechanics*, Vol. 55, 2003, pp. 39-89.
[37] Voyiadjis, G. Z., Abu Al-Rub, R. K., and Palazotto, A. N. "Thermodynamic Formulations for Non-Local Coupling of Viscoplasticity and Anisotropic Viscodamage for Dynamic Localization Problems Using Gradient Theory," *International Journal of Plasticity*, Vol. 20, 2004, pp. 981-1038.

[38] Abu Al-Rub, R. K., Voyiadjis, G. Z., and Palazotto, A. N. "A Micro-damage Model for High Velocity Impact Using Combined Viscosity and Gradient Localization Limiters," *Proceedings of the ASME Applied Mechanics Division*, Vol. 256, 2005, pp. 123-130.
[39] Deliktas B., Voyiadjis, G.Z., Palazotto, A.N. Simulation of perforation and penetration in metal matrix composite materials using coupled viscoplastic damage model. Composites: Part B 40 (2009) 434–442
[40] Voyiadjis, G.Z., Deliktas, B., Palazotto, A.N. Thermodynamically consistent coupled viscoplastic damage model for perforation and penetration in metal matrix composite materials. Composites: Part B 40 (2009) 427–433
[41] Needleman, A. "Material Rate Dependent and Mesh Sensitivity in Localization Problems," *Computer Methods in Applied Mechanics and Engineering*, Vol. 67, 1988, pp. 68-85.
[42] Loret, B., and Prevost, H. "Dynamics Strain Localization in Elasto-(Visco-)Plastic Solids, Part 1. General Formulation and One-Dimensional Examples," *Computer Methods in Applied Mechanics and Engineering*, Vol. 83, 1990, pp. 247-273.
[43] Sluys, L. J., "Wave Propagation, Localization and Dispersion in Softening Solids," Ph.D. Thesis, Delft University of Technology, Netherlands, 1992.
[44] Wang, W. M., Sluys, L. J., and de Borst, R., "Interaction Between Material Length Scale and Imperfection size for Localization Phenomena in Viscoplastic Media," *European Journal of Mechanics, A/Solids*, Vol. 15, No. 3, 1996, pp. 447-464.
[45] Molinari, A., "Collective Behavior and Spacing of Adiabatic Shear Bands," *Journal of Mechanics and Physics of Solids*, Vol. 45, 1997, pp. 1551–1575.
[46] Batra, R. C., and Kim, C. H., "Adiabatic Shear Banding in Elasticviscoplastic Nonpolar and Dipolar materials," *International Journal of Plasticity*, Vol. 6, 1999, pp. 127-141.
[47] Batra, R. C., and Chen, L., "Shear Band Spacing in Gradient-Dependent Thermoviscoplastic Materials," *Computational Mechanics*, Vol. 23, 1999, pp. 8-19.
[48] Batra, R. C., and Wei, Z. G., "Shear Bands Due to Heat Flux Prescribed at Boundaries," *International Journal of Plasticity*, Vol. 22, 2006, pp. 1–15.
[49] Chelluru, S.K., *Finite Element Simulation of Ballistic Impact of Metal and Composite Plates*, in *Mechanical Engineering*. 2007, Whichita State University. p. 101.
[50] Christiansen, E.L. and L. Friesen, *Penetration equations for thermal protection materials.* International Journal of Impact Engineering, 1997. **20**(1-5): p. 153-164.
[51] Abu Al-Rub, R. K., and Voyiadjis, G. Z. "Determination of the Material Intrinsic Length Scale of Gradient Plasticity Theory," *International Journal of Multiscale Computational Engineering*, Vol. 2, No. 3, 2004, pp. 377-400.
[52] Abu Al-Rub, R. K., and Voyiadjis, G. Z. "Analytical and Experimental Determination of the Material Intrinsic Length Scale of Strain Gradient Plasticity Theory from Micro- and Nano-Indentation Experiments," *International Journal of Plasticity*, Vol. 20, No. 6, 2004, pp. 1139-1182.

[53] Voyiadjis, G. Z., and Abu Al-Rub, R. K. “Gradient Plasticity Theory with a Variable Length Scale Parameter,” *International Journal of Solids and Structures*, Vol. 42, No. 14, 2005, pp. 3998-4029.
[54] Arsenlis, A., and Parks, D. M., “Crystallographic aspects of geometrically-necessary and statistically-stored dislocation density,” *Acta Materialia,* Vol. 47, 1999, pp. 1597-1611.
[55] Haque, M. A., and Saif, M. T. A., 2004. Deformation mechanisms in free-standing nanoscale thin films:A quantitative in situ transmission electron microscope study. Proceedings of the National Academy of Science of the United State of America.
[56] Voyiadjis, G. Z., Abu Al-Rub, R. K., and Palazotto, A. N. “On the Small and Finite Deformation Thermo-elasto-viscoplasticity Theory: Algorithmic and Computational Aspects,” *European Journal of Computational Mechanics,* Vol. 15, No. 7-8, 2006, pp. 945-987.
[57] Zhu, Y. Y., and Cescetto, S. “Fully Coupled Elasto-Visco-Plastic Damage Theory for Anisotropic Materials,” *International Journal of Solids and Structures*, Vol. 32, 1995, pp. 1607-1641.
[58] Abu Al-Rub, R. K., and Voyiadjis, G. Z. “A Direct Finite Element Implementation of the Gradient Plasticity Theory,” *International Journal for Numerical Methods in Engineering*, Vol. 63, No. 4, 2005, pp. 603–629.
[59] Voyiadjis, G. Z., and Abu Al-Rub, R. K. “A Finite Strain Plastic-Damage Model for High Velocity Impacts Using Combined Viscosity and Gradient Localization Limiters, Part II: Numerical Aspects and Simulations,” *International Journal of Damage Mechanics*, Vol. 15, No. 4, 2006, pp. 335–373.
[60] ABAQUS User Manual, Version 6.3, Habbitt, Karlsson and Sorensen, Inc: Providence, RI, 2003.
[61] Voyiadjis, G.Z., Abed, F.H., “Implicit Algorithm for Finite Deformation Hypoelasticity in FCC Metals,” *International Journal for Numerical Methods in Engineering*, Vol. 67, 2006, pp. 933-959.
[62] Abed, F.H., Voyiadjis, G.Z., “Adiabatic Shear Band Localizations in BCC Metals at High Strain Rates and Various Initial Temperatures,” *International Journal for Multiscale Computational Engineering*, Vol. 5, Issues 3-4, 2007, pp. 325-349.
[63] Nemat-Nasser, S., Isaacs, J.B., and Liu, M. (1998) “Microstructure of high-strain, high-strain-rate deformed tantalum,” *Acta Metallurgica*, 46: 1307-1325.
[64] Perez-Prado, M.T., Hines, J.A., and Vecchio, K.S. (2001) “Microstructural evolution in adiabatic shear bands in Ta and Ta-W alloys,” *Acta Materialia*, 49: 2905-2917.
[65] Bronkhorst, C.A., Cerreta, E.K., Xue, Q., Maudlin, P.J., Mason, T.A., and Gray, G.T. (2006) "An experimental and numerical study of the localization behavior of tanatlum and stainless steel," *International Journal of Plasticity*, 22: 1304-1335.
[66] Borvik, T., Hopperstad, O. S., Berstad, T., and Langseth, M. “Numerical Simulation of Plugging Failure in Ballistic Penetration,” *International Journal of Solids and Structures*, Vol. 38, 2001, pp. 6241-6264.
[67] Bai, Y., and Dodd, B, ‘Adiabatic Shear Localization: Occurrence, Theories and Applications,” Oxford, Pergamon Press, 1992.